Efficiency-speed tradeoff in slow-light silicon photonic modulators

Omid Jafari, *Student Member, IEEE*, Wei Shi, *Member, IEEE, Member, OSA* and Sophie LaRochelle, *Senior Member, IEEE, Fellow, OSA*

***Abstract*—The purpose of this paper is twofold. First, we discuss the efficiency-speed tradeoff in slow-light (SL) silicon photonic (SiP) modulators. For this, a comprehensive model for the electro-optic (EO) response of lumped-electrode SL Mach-Zehnder modulators (SL-MZMs) is presented. The model accuracy is verified by comparing it to experiments. Our analysis shows that slowing down the optical wave helps to enhance efficiency by increasing the interaction time between the optical wave and the uniform voltage across lumped electrodes, but at the cost of limiting the EO bandwidth. Then, we investigate SL-MZMs with traveling-wave (TW) electrodes whose dynamic interaction is predicted using a distributed circuit model. Having been solved by the finite-difference time-domain (FDTD) method, the model shows that TW SL-MZMs are capable of improving both efficiency and speed under an optimized SL effect. We also compare SL-MZMs with conventional MZMs (C-MZM) considering a figure of merit (FOM) that combines key parameters such as efficiency, loss, and EO bandwidth. We show that the additional loss of SL waveguides significantly impacts the preferred modulator choice at different baudrates. The second aim of this paper is to examine different design strategies to reduce V_π of C-MZMs in order to meet the requirement of COMS driver using 1) a longer phase shifter, 2) higher doping densities, and 3) the SL effect. It is shown that the SL effect provides the best overall performance among the three. Indeed, only the SL effect offers simultaneous improvement in V_π, footprint, and EO bandwidth; the other approaches provide V_π reduction but at the cost of reduced speed or enlarged footprint (or even both).**

***Index Terms*— Silicon photonic modulators, slow light effect, electro-optic bandwidth, modulation efficiency, V_π reduction.**

I. Introduction

SILICON modulators are one of the key components needed to provide cost-effective and energy-efficient photonic integration of optical transceivers [1], [2]. Tremendous efforts have recently been dedicated to improving the performance of SiP modulators. Notwithstanding, three fundamental tradeoffs still exist between: efficiency-stability, efficiency-speed, and efficiency-loss. The efficiency of modulators is described by either their V_π or power consumption in energy per bit.

Among SiP modulators, MZMs loaded with TW electrodes are preferred devices in commercial optical systems because of their stability and high-speed operation. However, they are generally energy-hungry and have a large footprint [3]–[6]. In contrast, resonator-based modulators, for example, micro-ring modulators (MRMs), offer a highly efficient operation with energy consumption of only a few femtojoule per bit and a compact footprint [7]–[12]. However, MRMs are unstable and sensitive to the operational wavelength. Moreover, their speed is limited by the photon lifetime of their cavities.

SL-MZMs recently demonstrated outstanding potential to improve SiP modulator efficiency and stability, simultaneously [13]–[21]. Indeed, slowing down the optical waves can enable significant modulation enhancement over a large optical bandwidth while offering an operating condition insensitive to temperature fluctuations. For instance, using 2-D photonic crystal waveguides loaded into an MZM, Ref. [13] reports a group index of about 10 over the whole C-band with a phase shifter length of 200 μm. In Ref. [16], micro-ring resonators are used to slow down optical waves inside an MZM and the authors report an operating temperature range of 54 ^{0}C with a compact phase shifter length of 110 μm and an enhancement factor of γ= 8. Here, the enhancement factor is defined as $\gamma=n_{g,SL}/n_g$, where $n_{g,SL}$ and $n_g \sim 3.8$ are the group indices of SL waveguides and simple waveguides, respectively. In Ref. [20], an MZM based on 1-D photonic crystal (Bragg grating) waveguides was proposed. This modulator is characterized by a group index of 8 over an optical bandwidth of 1.3 nm with a footprint length of 500 μm. We recently demonstrated an MZM assisted by Bragg grating resonators, which achieved γ= 7 over an optical bandwidth of 3.5 nm (equivalent to an operating temperature range of ~ 40 ^{0}C) with a phase shifter length of 162 μm [21].

Although SL-MZMs are capable of enhancing both efficiency and stability, their operating speed is typically limited. Conventional SiP modulators (such as MRMs and MZMs) are characterized by an efficiency-speed tradeoff: modulation efficiency is enhanced either by increasing p-n junction capacitance or photon lifetime at the cost of compromised EO bandwidth. In the case of SL-MZMs, because of their short phase shifter, they are typically implemented with lumped electrodes and their speed is restricted not only by the RC time constant but also by the interaction time between the optical signal and the uniform voltage along electrodes ([22], [23]). This interaction time is increased by the low optical group velocity. The SL effect therefore imposes an intrinsic restriction on the modulator speed. Studies show that specially designed

Centre d'optique, photonique et laser (COPL), Department of Electrical and Computer Engineering, Université Laval, Québec, QC, G1V 0A6, Canada (e-mail: omid.jafari.1@ulaval.ca; wei.shi@gel.ulaval.ca; sophie.larochelle@gel.ulaval.ca)

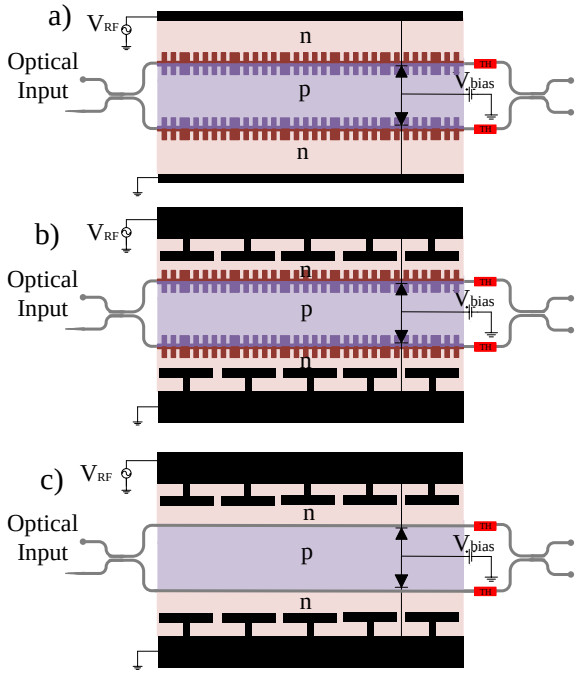

Fig. 1. Schematic of a SL-MZM based on Bragg grating resonators and a) lumped electrodes, and b) TW electrodes. A C-MZM with TW electrodes is shown in c).

TW electrodes can mitigate this issue. For example, in Ref. [24], a SL-MZM combined with meander-line electrodes was proposed to compensate for the velocity mismatch between RF and optical waves.

In order to investigate the efficiency-speed tradeoff in SL-MZMs, a deeper understanding of the dynamic interaction between electrical and optical waves in SL-MZMs is required. Many efforts have been dedicated to modeling lumped-electrode modulators [22], [25]–[27], and TW MZMs [28]–[31]; however, none of these previous models incorporated the SL effect. In this paper, we present and experimentally validate a dynamic model for SL-MZMs combined either with lumped electrodes or with TW electrodes. Such a model is currently missing from the literature. We investigate the EO response of SL-MZMs in comparison to C-MZMs considering efficiency, loss, and EO bandwidth.

The rest of the paper is organized as follows. In Section II, we first develop a model to predict the EO response of lumped-electrode SL-MZMs, as shown in Fig. 1 (a). We validate the model with experimental measurement. Thereafter in Section III, we expand the model for SL-MZMs to include TW electrodes as illustrated in Fig. 1 (b). The model is obtained by solving the coupled equations of TW electrodes using the FDTD method. Afterwards, we compare the three modulators: lumped-electrode SL-MZM, TW SL-MZM, and C-MZM shown in Fig. 1 (c). We consider the EO bandwidth and a FOM that combines performance indicators such as efficiency, loss, and EO bandwidth. Finally, in Section IV, we examine and discuss three design strategies to reduce V_π of MZMs: increasing the phase shifter length (IPSE), increasing doping density (IDD) of p-n junctions, and using the SL effect.

II. SL-MZM WITH LUMPED ELECTRODES

A. EO Model

In this section, we develop a general model of the EO response of lumped-electrode SL-MZMs with analysis of both RF circuit and optical waveguide. The model can be employed for SL-MZMs based on different passive structures. In this paper, our case study is the lumped-electrode SL-MZM based on Bragg grating resonators (BGRs) reported in [21] (shown Fig. 1 (a)). In [32], we explained in detail how to engineer the SL effect using Bragg grating resonators.

RF analysis: An equivalent electrical circuit for a loaded transmission line (TML) is required to calculate the effective RF power applied on p-n junctions. Fig. 2 shows the cross-section of the modulator operated with the single-drive push-pull configuration, as well as its equivalent electrical circuit [22], [26], [27]. The impedance mismatch between the TML and the RF source introduces a RF transmission coefficient (T_{TML}) as

$$T_{TML}(\omega)=\frac{2\left[\left(j\omega L+2R_{PN}+2\left(j\omega C_{PN}\right)^{-1}\right)^{-1}+j\omega C_0\right]^{-1}}{\left[\left(j\omega L+2R_{PN}+2\left(j\omega C_{PN}\right)^{-1}\right)^{-1}+j\omega C_0\right]^{-1}+Z_0} \quad (1)$$

where C_{PN} and R_{PN} are capacitance and series resistance of a single p-n junction, respectively. L represents the electrode inductance. C_0 is the pad parasitic capacitance. The characteristic impedance of the source is represented by Z_0. After that, the effective voltage (V_{eff}) on each p-n junction as a function of the source (V_{RF}) is calculated as

$$V_{eff}(\omega)=\frac{1}{2}\frac{2\big/j\omega C_{PN}}{j\omega L+2R_{PN}+2\big/j\omega C_{PN}}T_{TML}(\omega)V_{RF}(\omega)$$
$$=T_{Circuit}(\omega)T_{TML}(\omega)V_{RF}(\omega) \quad (2)$$

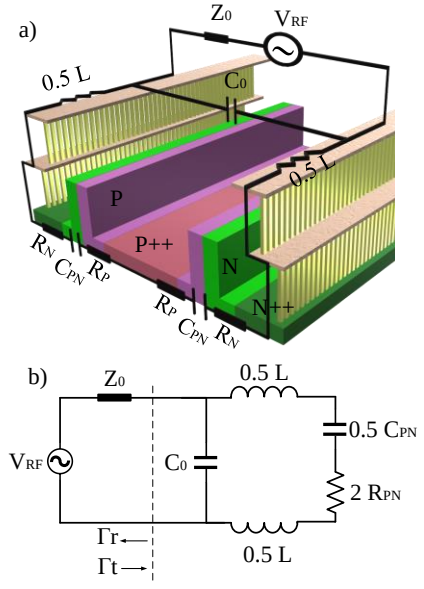

Fig. 2. a) Schematic of a single-drive push-pull MZM with lumped electrodes. b) Equivalent RF circuit model.

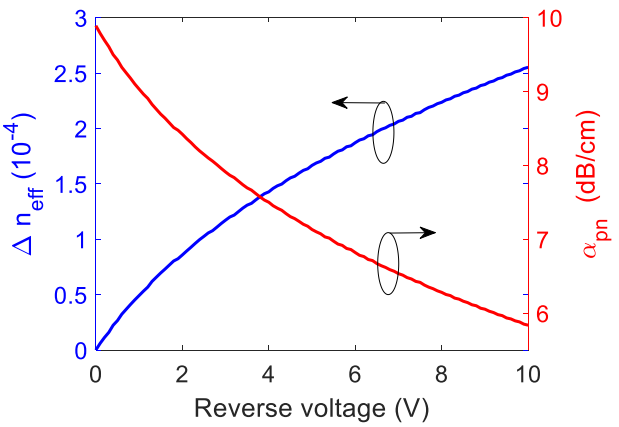

Fig. 3. The changes in the refractive index and the p-n junction absorption loss as a function of reverse voltage for a simple waveguide.

Optical analysis: In this step, we derive an expression of the optical phase shift, produced by carrier depletion in the p-n junction, as a function of the effective voltage. The changes in the effective index due to the applied voltage is given as

$$\Delta n_{eff}(V(\omega)) = \frac{\iint E^*(x,y)\Delta n(x,y,V(\omega))E(x,y)\,ds}{\iint E^*(x,y)E(x,y)\,ds} \tag{3}$$

where E is the mode electrical field, and Δn is described as [33]

$$\Delta n(x,y,V) = -3.64\times10^{-10}\lambda^2\Delta N_D(x,y,V) - 3.51\times10^{-10}\lambda^2\Delta N_A{}^{0.8}(x,y,V) \tag{4}$$

where λ is the optical wavelength, and ΔN_A and ΔN_D are the carrier densities of holes and electrons, respectively. We simulate the electrical field for the fundamental optical waveguide mode in a rib waveguide using Lumerical-Mode. Afterward, we numerically compute the integrals in Eq. (3) using MatLab to calculate the changes in the refractive index as a function of the effective voltage, as shown in Fig. 3 (blue line) [25], [31], [32]. Note that the values of all parameters are presented in Table II of Appendix I.

The partial derivative of the phase shift ($\delta\Delta\varphi$) is calculated along a very small length of the electrode ($\delta L_{SL\text{-}MZM}$) as $\delta\Delta\varphi(V(t))=k_0\times\Delta n(V(t))\times\delta L_{SL\text{-}MZM}$, where k_0 is equal to $2\pi/\lambda$. Considering that light speed is constant along the waveguide, $\delta L_{SL\text{-}MZM}$ can be expressed as $\delta L_{SL\text{-}MZM}=(c/\gamma n_g)\times\delta t$, where c is the light speed in free space. Finally, the total phase shift along the electrode is computed as

$$\Delta\varphi(V(t)) = k_0\frac{c}{\gamma n_g}\int_{t-t_0}^{t}\Delta n_{eff}(V(t))\,dt, \quad t_0 = \frac{\gamma n_g L_{SL-MZM}}{c} \tag{5}$$

The time-dependent phase shift expressed in Eq. (5) can be expressed in the frequency domain as (see Appendix II)

$$\Delta\varphi(V(\omega)) = k_0\frac{c}{\gamma n_g}\left(1-e^{-j\omega t_0}\right)\times \left[\Delta n_{eff}(V(\omega))\times\left(\frac{1}{j\omega}+\pi\delta(\omega)\right)\right] \tag{6}$$

Considering an MZM operated at the quadrature point, the frequency response, S_{21}, of SL-MZMs is now derived as (see Appendix III)

$$|S_{21}(\omega)|^2 = \frac{e^{-\alpha L}}{2}\mathbf{F}\left\{\sin\left(\mathbf{F}^{-1}\left[\Delta\varphi(V,\omega)\right]\right)\right\} \tag{7}$$

where $\mathbf{F}$ and $\mathbf{F}^{-1}$ represent the Fourier- and inverse-Fourier transform, respectively, and α is the attenuation coefficient.

B. Model Validation

We verify our model using measurement results of an MZM assisted by BGRs reported in Ref. [21]. Each arm of the MZM is loaded with BGR having six-coupled resonators. Each resonator consists of a phase-shifted section with 45 grating periods on each side. The key idea in this design was to keep the resonance bandwidth wide by employing coupled cavities with a low-quality factor. The modulator demonstrates an enhancement factor of γ= 7 over an optical bandwidth of about 3.5 nm with a phase shifter length of $L_{SL\text{-}MZM}$= 162 μm. The colored dashed lines in Fig. 4 show the measured $|S_{21}|$ for different operational wavelengths with 3-dB bandwidths close to 28 GHz at a reverse bias of 1 V. The solid black line in Fig. 4 illustrates the EO response of the SL-MZM predicted by our model, showing a good agreement with the measurement. We also perform a large-signal analysis and plot the optical eye diagram in Fig. 5 (a). These simulations considered a peak-to-peak voltage of 3.5 V on each arm, a reverse bias voltage of 1.5 V, an operational wavelength of 1570 nm, and a modulation speed of 20 Gb/s. Comparing it with Fig. 5 (b), the model provides a satisfactory estimation of the measured eye diagram reported in [21].

C. EO Bandwidth of SL Modulators with Lumped Electrodes

After obtaining a reliable model, we perform an analysis to understand the impact of the enhancement factor and the bias voltage on the EO bandwidth of lumped-electrode SL-MZMs. Fig. 6 shows the EO bandwidth of SL-MZMs with a phase shifter length of $L_{SL\text{-}MZM}$= 162 μm as a function of the reverse bias (V_{bias}) for different enhancement factors. As expected, the EO bandwidth increases as V_{bias} becomes larger; however, the increase is inversely related to the enhancement factor. In other words, as V_{bias} changes from 0 V to -20 V, the increase for γ= 3 is 33 GHz, whereas it is 3.1 GHz for γ= 13. Indeed, if a strong SL effect is exploited, the EO bandwidth saturates as it becomes limited by the interaction time. It is also seen that for larger enhancement factors, the EO bandwidth saturates at lower V_{bias}; i.e. the saturation voltage is 10 V for γ= 7, whereas it is 6 V for γ= 10.

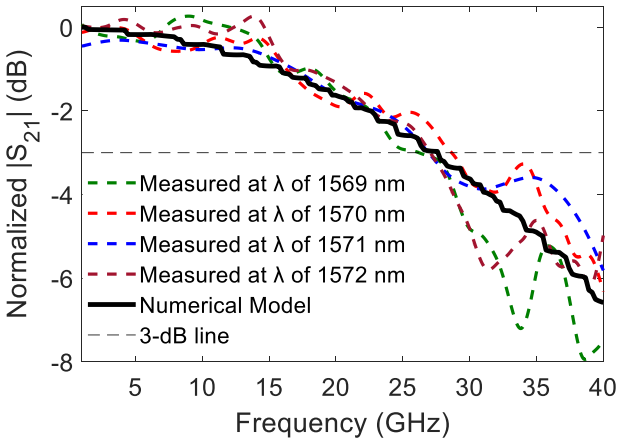

Fig. 4. Normalized S_{21} of SL-MZM with lumped electrodes (γ= 7, V_{bias}= -1 V and $L_{SL\text{-}MZM}$= 162 µm). Dash-colored lines are measurement results for different operational wavelengths. The solid black line is the EO response predicted by the model.

D. Comparing SL-MZMs to C-MZMs

We compare the performance of SL-MZMs with lumped electrodes to a C-MZM with TW electrodes, by considering the EO bandwidth as well as a FOM introduced in [34]. In Ref. [35], an MZMs with TW electrodes was designed and demonstrated for operation above 400 Gb/s. This modulator is characterized by a V_π~ 7 V, a phase shifter length of $L_{C\text{-}MZM}$= 4.8 mm, and an insertion loss of 12.3 dB/cm, including the propagation loss (~2.5 dB/cm) and the absorption loss (~9.8 dB/cm). Utilizing the time-domain model reported in [31], we estimate this MZM EO bandwidth as 15.8 GHz at V_{bias} of -1 V. We choose this modulator as a reference in our analysis.

SL-MZMs are typically characterized by high insertion loss of more than 100 dB/cm, which is caused by the highly structured passive SL waveguides that generate loss through sidewall roughness and lithographic inaccuracies. This loss typically scales with group index. We reported an insertion loss of 123 dB/cm for a γ= 7 MZM assisted by BGRs [21]. In [36], [37], it is shown that the propagation loss in SL waveguides scales linearly with γ and, therefore, we assume in our assessment that the proportionality factor is 17.5 dB/cm (e. g., $\alpha_{SL\text{-}MZM}$= 35 dB/cm for γ= 2).

To make a fair comparison, we consider an operating condition under which both modulators (SL-MZMs and the C-MZM) possess similar V_π. To this end, the phase-shifter length of the C-MZM must be equal to the length of SL-MZMs multiplied by the enhancement factor, as expressed in Eq. (8) or, in the following analysis, $L_{C\text{-}MZM}$= 4.8 mm and $L_{SL\text{-}MZM}$= *4.8/*γ mm. Also, note that we set V_{bias}= -1 V for all calculations.

$$L_{C-MZM} = L_{SL-MZM} \times \gamma \tag{8}$$

1) EO Bandwidth

The calculated EO bandwidth of the SL-MZMs with lumped electrodes and the C-MZM with TW electrodes, under the condition of Eq. (8), are shown in Fig. 7. As mentioned previously, the EO bandwidth of the C-MZM is 15.8 GHz,

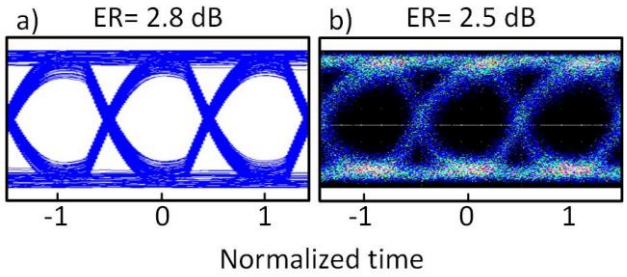

Fig. 5. Eye diagram of SL-MZM with lumped electrodes at 20 Gb/s a) simulation b) measurement with V_{pp}=3.5 V on each arm, V_{bias}=1.5 V and λ=1570 nm.

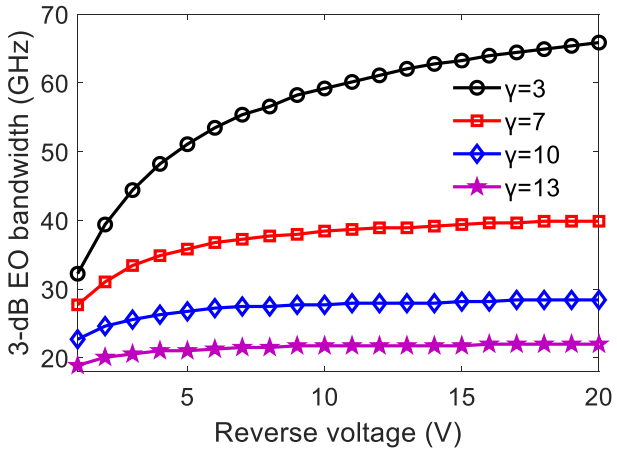

Fig. 6. The EO bandwidth as a function of reverse voltage for different enhancement factors and $L_{SL\text{-}MZM}$= 162 µm.

while the "SL-MZM" with lumped electrode and no SL effect (γ= 1 and $L_{SL\text{-}MZM}$= 4.8 mm) provides only a 6 GHz bandwidth. When slowing down the light (γ > 1), the EO bandwidth first improves and then saturates. Up to γ= 5 ($L_{SL\text{-}MZM}$= 960 µm), the EO bandwidth is increased to 9 GHz and, thereafter, it remains almost unchanged. Indeed, larger enhancement factors ($\gamma \geq 5$) allow a reduction in the phase shifter length and, consequently, a decrease in the RC time constant; however, this comes at the cost of an increase in the interaction time. The reduction in the RC constant and the increase in the interaction time compensate each other, resulting in an EO bandwidth that remains fixed.

It is also observed in Fig. 7 that the C-MZM offers an EO response with a smooth roll-off, which is a key advantage to operate modulators at much larger baudrate than their EO bandwidth. In the present case, the 10-dB bandwidth is 33 GHz for the C-MZM, whereas it is only 14.5 GHz for SL-MZM with γ= 9 ($L_{SL\text{-}MZM}$= 533 µm).

2) FOM

A SiP modulator FOM grouping efficiency, loss, and EO bandwidth was derived in [34]. A classical FOM is FOM=$V_\pi \alpha L_{PS}$, where L_{PS} is the phase shifter length. This FOM is derived considering the static transmission power penalty (TPP) generated by the modulation loss and the propagation loss. In addition to this static TPP, a dynamic TPP occurs due to intersymbol interference (ISI) resulting from the finite EO bandwidth. The impact of ISI is particularly important when modulators operate at baudrate exceeding their EO bandwidth.

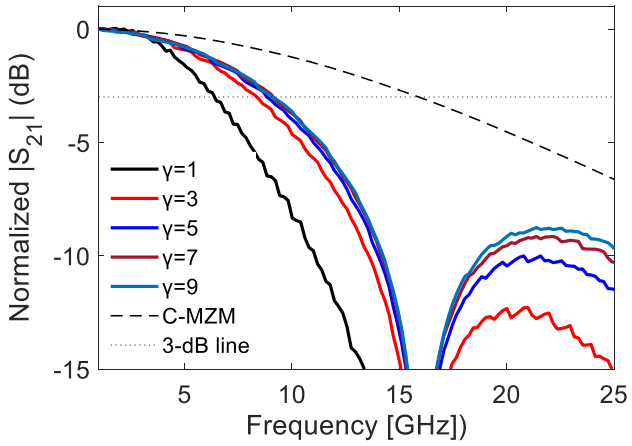

Fig. 7. Normalized S_{21} for SL-MZMs with lumped electrodes and the C-MZM. $L_{C\text{-}MZM}$= 4.8 mm, $L_{SL\text{-}MZM}$= 4.8/γ mm, and V_{bias}= -1 V.

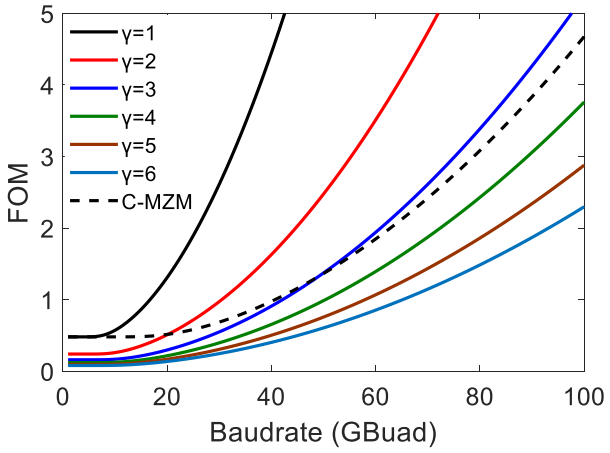

Fig. 8. FOM for OOK modulation format (M= 2), without considering loss (α=1 dB/cm for both cases), as a function of baudrate for lumped-electrode SL-MZMs and the C-MZM. $L_{C\text{-}MZM}$= 4.8 mm, $L_{SL\text{-}MZM}$= 4.8/γ mm, V_{bias}= -1 V.

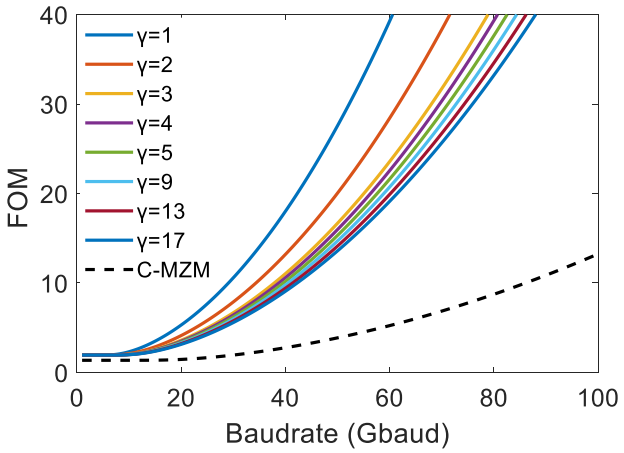

Fig. 9. FOM for OOK modulation format (M= 2), considering loss (α= 12.5 dB/cm for C-MZM and α= 17.5×γ dB/cm), as a function of the baudrate for lumped-electrode SL-MZMs and the C-MZM. $L_{C\text{-}MZM}$= 4.8 mm, $L_{SL\text{-}MZM}$= 4.8/γ mm, and V_{bias}= -1 V.

The classical aforementioned FOM does not take this into account. In Ref. [34], it was theoretically shown that the normalized optical modulation amplitude (OMA) is a more reliable means to represent the dynamic and static TPPs. From the definition of OMA, the authors add another term to the FOM, that is now as expressed as

$$FOM = V_\pi \alpha L_{PS} \frac{M-1}{1-\frac{M}{2}.\exp\left(-4.43\frac{BW_{EO}^2}{BR^2}\right)} \quad (9)$$

where BW_{EO} is the EO bandwidth, BR the target baudrate, and M is the modulation level of the modulation format. For future discussion, note that smaller FOM indicates better performance.

We carry out our FOM analysis with and without loss in order to examine its impact on the performance of SL-MZMs. Fig. 8 illustrates the FOM for the C-MZM (dash line) and lumped-electrode SL-MZMs (solid lines) with different γ as a function of baudrate without including loss (α= 1 dB/cm for both cases). As depicted, lumped-electrode SL-MZMs demonstrate superior performance if the light is slowed down enough ($\gamma \geq 4$). Indeed, larger enhancement factors ($\gamma \geq 4$) make phase shifter more compact ($L_{SL\text{-}MZM} \leq 1.2$ mm), which leads to a drastic reduction in the FOM's value. Including the excess loss due to the SL waveguide in the evaluation has an important impact in the lumped-electrode SL-MZMs FOM, as shown in Fig. 9 (i.e., α= 12.5 dB/cm for C-MZM and α= 17.5×γ dB/cm). The SL-MZM no longer presents a better performance, even with strong SL effects. The two FOMs are diverging rapidly for baudrates >20 Gbaud and, for example, at baudrate of 80 Gbaud, the $FOM_{C\text{-}MZM}$ is 8.7, whereas the $FOM_{SL\text{-}MZM}$ is 36 under with γ= 9 ($L_{SL\text{-}MZM}$= 533 µm).

E. Discussion: Lumped-Electrode SL-MZMs vs C-MZMs

The C-MZM offers a larger EO bandwidth than lumped-electrode SL-MZMs (under the condition of Eq. (8)). Furthermore, the EO response of C-MZM is more suitable to push the operation to high baudrate due to its smooth frequency response roll-off. As a result, lumped-electrode SL-MZMs enhance efficiency but at the cost of reduced speed. These modulators therefore do not present a solution to the efficiency-speed tradeoff. One way to improve the performance of SL-MZMs is to optimize their passive structures and the fabrication processes to reduce the excess loss of SL waveguides, which is out of the scope of this paper. Another way is to manipulate the electrodes in order to improve the EO bandwidth, which will be discussed in the following section.

III. SL-MZMs WITH TW ELECTRODES

In this section, we investigate SL-MZMs with TW electrodes (Fig. 1 (b)) and examine whether TW electrodes enable SL-MZMs to address the efficiency-speed tradeoff and present an improved performance compared to C-MZMs.

A. Small Signal Model for TW SL-MZMs

In Ref. [31], a comprehensive time-domain model for C-MZMs with TW electrodes is reported. We now expand this model such that it also incorporates the SL effect. The model is based

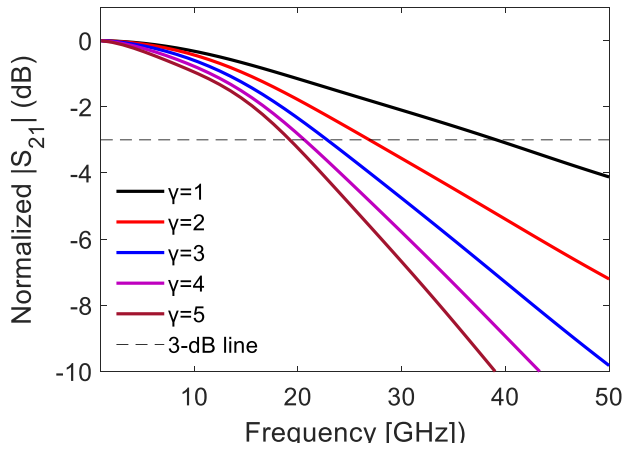

Fig. 10. EO response of SL-MZMs combined with TW electrodes with $L_{SL\text{-}MZM}$ = 1 mm at a reverse bias of 1 V.

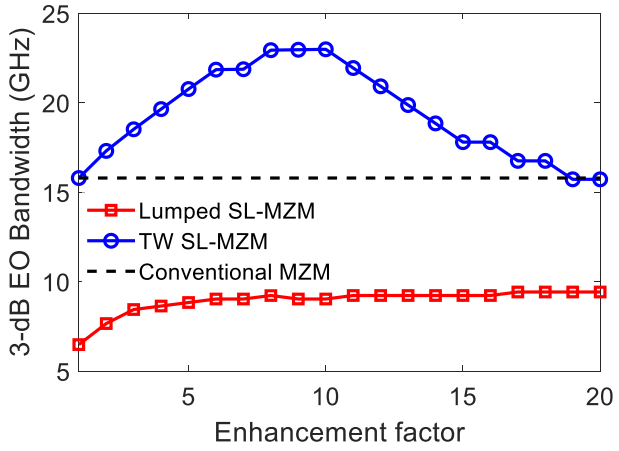

Fig. 11. The EO bandwidth as a function of enhancement factor at the reverse voltages of 1 V. $L_{C\text{-}MZM}$= 4.8 mm, and $L_{SL\text{-}MZM}$= 4.8/γ mm.

on coupled propagation equations of the forward and backward RF waves along the TML [31]. Solved by the FDTD method (see Appendix IV), the model records the forward and backward RF signals on the finite-difference mesh with a step size of ΔZ_{RF} in time steps of Δt. To consider the velocity mismatch between optical and electrical waves in the simulation, the following conditions should be satisfied.

$$\Delta Z_{RF} = \frac{n_g \gamma}{n_{RF}} \Delta Z_{Opt}, \quad \Delta t = \frac{n_g \gamma}{c} \Delta Z_{Opt} \tag{10}$$

where ΔZ_{Opt} is the optical mesh size and n_{RF} is the RF index, which is taken as 2.7 for TW electrodes [5], [31].

Fig. 10 shows the EO response of a TW SL-MZM with a fixed phase shifter length of 1 mm for different enhancement factors. As can be seen, the TW MZM with no SL effect (γ = 1) provides an EO bandwidth of about 40 GHz, while the TW SL-MZM with γ = 5 presents a bandwidth of around 20 GHz. This reduction in the EO bandwidth comes from the increased velocity mismatch between the electrical and optical signals when the light is slowed down.

B. Comparing TW SL-MZMs with C-MZMs

In this section, similarly to the section II-D, we compare a TW SL-MZM to the C-MZM considering the EO bandwidth and the FOM. As was done previously, the respective lengths of the MZM structures are chosen in accordance to Eq. (8).

1) EO Bandwidth

Figure 11 shows the EO bandwidth estimated for lumped-electrode SL-MZMs and TW SL-MZMs as a function of the enhancement factor. We also plot the 3-dB bandwidth of the C-MZM as a reference value (black dash line). As can be seen, the TW SL-MZM offers a larger EO bandwidth compared to C-MZM in a specific range of the enhancement factor. In this range, TW SL-MZM require shorter electrodes to operate with the same V_π, which leads to a reduction in the RF attenuation. The small length and the reasonable SL effect ($\gamma \sim 9$) also limit the EO velocity mismatch.

Fig. 11 also indicates that the EO bandwidth reaches a maximum at an optimum enhancement factor of γ = 9 ($L_{SL\text{-}MZM}$= 533 µm). The optimum γ represent a compromise between the two limiting factors of the EO bandwidth (RF loss and EO velocity mismatch), for γ < 9 the EO bandwidth is limited by the RF loss and while its limited by the EO velocity mismatch γ > 9. In Fig. 12, we examine the EO bandwidth for different V_{bias}, showing that the optimum γ is voltage-dependent and shifts to larger value with increasing V_{bias}, i.e., the optimum values are γ= 9, 12, 14, and 16 at V_{bias}= -1 V, -2 V, -3 V, and -4 V, respectively.

Finally, Fig. 11 illustrates that the substitution of lumped electrodes by TW electrodes allows a significant improvement in the EO bandwidth of SL-MZMs. For example, at γ= 9 ($L_{SL\text{-}MZM}$ = 533 µm), the TW SL-MZM offers a 23 GHz bandwidth, while it is only 9 GHz for the lumped-electrode SL-MZM.

2) FOM

We evaluate the FOM expressed in Eq. (9) for the TW SL-MZMs and the C-MZM. Fig 13 (a) shows the results without including loss in the analysis (α= 1 dB/cm for both cases). The TW SL-MZM, for all γ, outperforms the C-MZM in terms of efficiency and EO bandwidth. This is because the TW SL-MZM requires a shorter length for the same V_π (e.g., $L_{SL\text{-}MZM}$= 0.96 mm at γ= 5 vs. $L_{C\text{-}MZM}$ = 4.8 mm), and provides a larger EO bandwidth (for example, $f_{SL\text{-}MZM}$ = 20.7 GHz at γ= 5 vs. $f_{C\text{-}MZM}$ = 15.8 GHz).

In Fig. 13 (b), showing both FOMs in the presence of the loss, when the light is not slowed down enough (γ= 3) or is slowed down too much (γ= 15), the C-MZM still outperforms TW SL-MZMs at all baudrates. The reason is that for γ= 3, the long length of the phase shifter results in a high RF loss; and for γ= 15, the velocity mismatch between the RF and optical waves is too large. On the other hand, if the light speed is reduced by factors of 5 to 13 ($5 \leq \gamma \leq 13$), the best modulator depends on the target speed (baudrate); for example, considering γ= 9, the C-MZM operates better at lower speed (<35 Gbaud), while it is the TW SL-MZM for higher speed (>35 Gbaud). Indeed, for baudrates below 35 Gbaud, the additional loss associated with

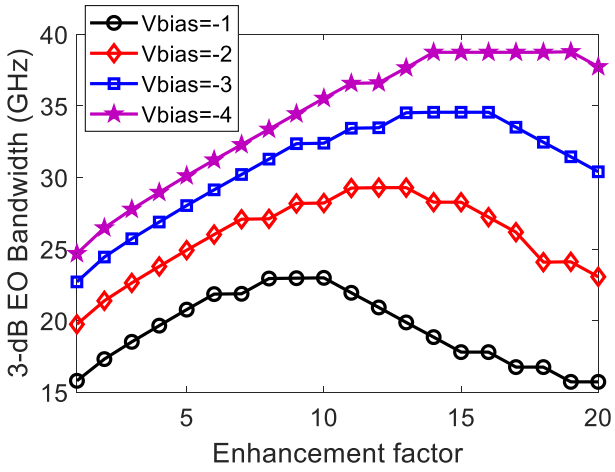

Fig. 12. EO bandwidth of SL-MZMs with TW electrodes as a function of the enhancement factor for different V_{bias}. $L_{SL\text{-}MZM}$= 4.8 mm, and $L_{SL\text{-}MZM}$= 4.8/γ mm.

SL waveguides does not allow the total TPP of the SL-MZM to become smaller than the one of the C-MZM. On the other hand, for high-speed operations (>35 Gbaud), the EO bandwidth is the determining factor to minimize the total TPP, and thus the TW SL-MZM demonstrates superior performance.

Finally, Fig. 13 (b) shows that the optimum γ defined in the previous section (γ= 9), demonstrates the lowest FOM for high baudrates in this case as well. Considering now a modulation speed of 100 Gbaud, which is being targeted for designing the next generation of SiP transmitters, the C-MZM presents the FOM of 13.25, whereas the TW SL-MZM reduces this value by 3.75, i.e., $FOM_{SL\text{-}MZM}$= 9.5.

C. *Discussion: TW SL-MZMs vs. C-MZMs*

TW SL-MZMs can exhibit significant improvement in both efficiency and speed. At the optimum enhancement factor, they improve the EO bandwidth by 7.5 GHz due to their much reduced length for the same V_π. Therefore, SL-MZMs with TW electrodes offers a solution to the efficiency-speed tradeoff. As shown in Fig. 13 (b), the TW SL-MZM under an optimum design is a promising candidate to substitute the C-MZM. Indeed, despite the additional loss associated with SL waveguides, TW SL-MZMs reduces the total TPPs compared to C-MZMs because of their large EO bandwidth.

IV. V_Π Reduction in SiP MZMs

Due to constraints in CMOS drivers and electrical interfaces, the required swing voltage for driving SiP modulators should be as low as possible [38]. Indeed, implementation of CMOS drivers with swing voltages of more than 2.5 V is very challenging because of the reliability concerns although there are some demonstrations on co-design SiP modulators with a high-swing CMOS driver [39]–[41]. In addition, the high RF propagation loss at high-speed operations (>50Gbaud) is an important limitation to bandwidth scaling that can be somewhat relaxed by a reduction in the electrical power budget [38]. It is therefore of high interest to reduce the energy per bit consumption (E_b) of SiP modulators, which scales with the peak-to-peak voltage (i.e., $E_b \propto V_{pp}^2$).

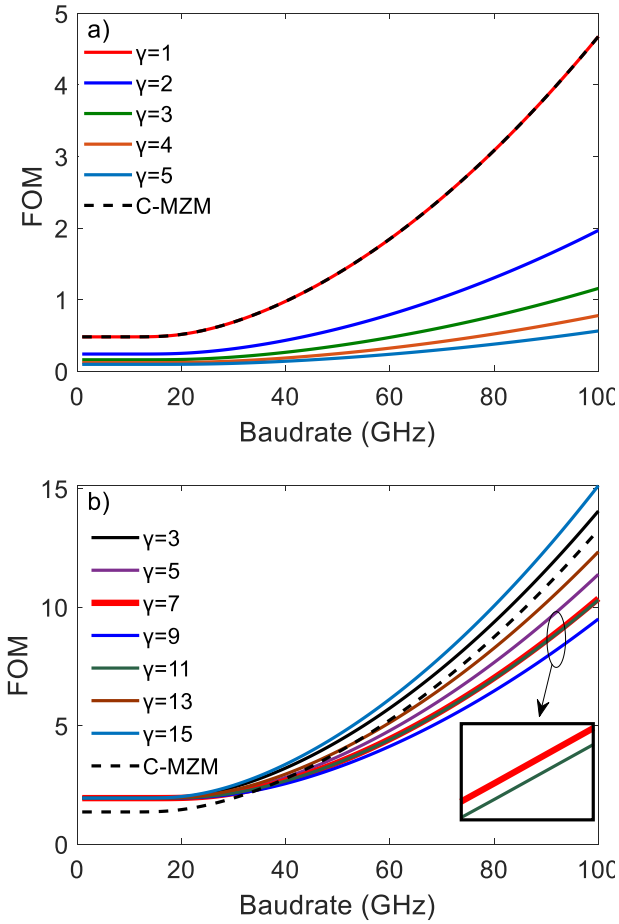

Fig. 13. FOM for OOK modulation format (M= 2) a) without b) with considering loss of the SL waveguides as a function of baudrate for TW SL-MZM and the C-MZM. $L_{SL\text{-}MZM}$= 4.8 mm, $L_{SL\text{-}MZM}$= 4.8/γ mm, and V_{bias}= -1 V.

Improvement in SiP modulators V_π requirements is thus necessary for high-performance integration system. The C-MZM in our study was characterized by a V_π of 7 V with a length of L_{PS}= 4.8 mm, which is not compatible with current CMOS drivers. For example, in [42], the authors have reported a modulator driver with a peak-to-peak voltage of 2.5 V using a partially depleted SOI 45-nm process. In order to meet this voltage range, the aforementioned V_π should reduce by a factor of 3 (i.e., V_π= 2.33 V). Three design strategies are examined below.

A. *Design Strategies to Reduce V_π*

1) *Increasing phase shifter length (IPSL)*

Considering the phase shift equation (π=k_0×$\Delta n(V_\pi)$×$L_{C\text{-}MZM}$), the easiest way to reduce the V_π is to make phase shifters longer. According to the index variation versus the applied voltage shown in Fig. 3, the C-MZM will offer a V_π of 2.33 V if its length increases by a factor of about two (i.e., $L_{C\text{-}MZM}$= 10 mm).

2) *Increasing doping density (IDD)*

Increasing the doing level allows an enhancement in the efficiency of phase shifters [12]. For example, our studied devices (the lumped-electrode SL-MZM and the C-MZM) have

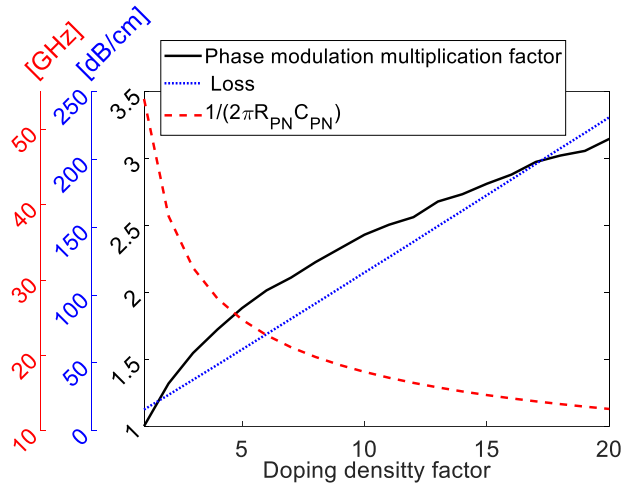

Fig. 14. Phase modulation multiplication factor, total loss, and RC constant of a simple p-n junction as a function of the normalized doping density factor (a normalized doping density factor of 5 means doping concentrations of $5\times N_A$ and $5\times N_D$ with N_A= 5×10^{17} cm^{-3} and N_D= 3×10^{17} cm^{-3}).

been fabricated under an estimated doping concentrations of N_A= 5×10^{17} cm^{-3} and N_D= 3×10^{17} cm^{-3} for holes and electrons, respectively [34]. When the doping level increases as shown in Fig. 14, an enhancement in the phase modulation is achieved but at the cost of significantly increased loss and reduced RC-bandwidth. According to Fig. 14, in order to reduce the V_π from 7 V to 2.33 V, the doping density of the C-MZM with TW electrodes should increase by a factor of 6, which would increase the phase modulation by a factor of 2 (i.e., N_A= 30×10^{17} cm^{-3} and N_D=18×10^{17} cm^{-3}).

3) *SL effect*

As discussed in this paper, the SL effect is another means to decrease the V_π. According to the phase shift equation ($\pi=k_0\times\Delta n(V_\pi)\times\gamma\times L_{SL\text{-}MZM}$), a SL-MZM loaded by TW electrode with an optimized enhancement factor of γ= 12 and a phase shifter length of $L_{SL\text{-}MZM}$ = 833 µm offers a V_π of 2.33 V.

B. *Discussion*

Table I compares the performance characteristics of these various approaches considering EO bandwidth, loss, and phase shifter length. As shown, the IPSL is not an effective way to lessen the V_π because it leads to a significantly reduced bandwidth. Indeed, with exploiting this approach, the EO bandwidth shrinks due to the RF loss, moreover the footprint is increased. The IDD approach provides a low V_π of 2.33 V with the same phase shifter length as the C-MZM, but at the cost of introducing a significant loss (33 dB) mainly originated by the absorption loss of p-n junctions, as well as a dramatically shrunk EO bandwidth due to the heavy doping that increases the conductor loss and the dielectric loss considerably, resulting in increased RF loss [35]. On the other side, the SL-MZM combined with TW electrodes is capable of reducing V_π from 7 V to 2.33 V, improving the EO bandwidth from 15.8 to 17.6 GHz, as well as shortening the phase shifter from 4.8 mm to 833 µm. Compared to the IDD scheme, the SL design also offers a better compromise on loss (17 dB vs. 33 dB). Finally, we examine the three approaches considering the FOM expressed in Eq. (9). The simulation results are shown in Fig. 15. As can be seen, the SL approach presents the optimum FOM compared to the other approaches. For example, at the 80 Gbaud, the FOM's values are 35.34, 238.5, and 21 for the IPSL, the IDD, and the SL effect approaches, respectively.

Table. I. Comparing different design strategies based on their operating parameters

	Reference MZM [35]	IPSL	IDD	SL effect
V_π (V)	7	2.33	2.33	2.33
EO bandwidth (GHz)	15.8	11.8	6.9	17.6
Phase shifter length (mm)	4.8	10	4.8	0.833
Loss (dB)	5.9	12.3	33	17

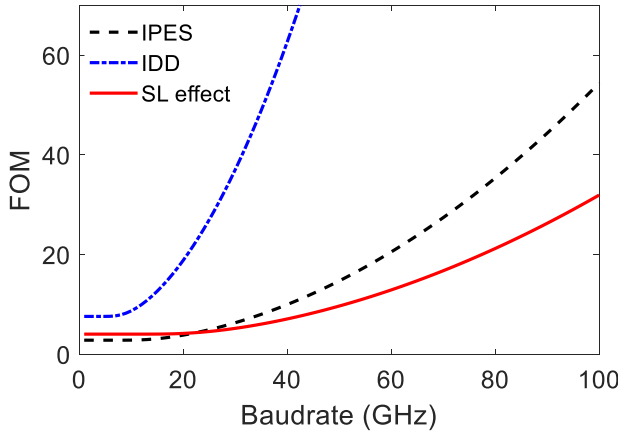

Fig. 15. FOM of the different approaches for V_π reduction through phase modulation enhancement as a function of the baudrate.

Recently, the IDD approach was used to bring down $V_\pi L_{PS}$ of SiP C-MZMs [38]. However, according to our assessment, using the SL waveguide with an optimized enhancement factor is a better solution for this purpose. As discussed, the SL approach not only improves significantly efficiency under a stable operation but also provides a larger EO bandwidth. On the other hand, the slight improvement in the efficiency using the IDD approach is provided at the expense of a dramatic reduction in EO bandwidth and severe increment in the absorption loss of p-n junctions.

The next generation of the integrated SiP platform should leverage TW SL-MZMs to enable a new class of SiP transmitters that feature best-in-class performance in key parameters such as high stability, low power budget, high EO bandwidth, and compact footprint. These modulators are capable of providing a very low V_π (< 2.5 V) with a compact phase shifter length (<1mm). Therefore, the requirements on the RF amplification and the thermal control are significantly relaxed, leading to reduced cost and complexity of control circuits and CMOS drivers. The additional loss associated with SL waveguides can be compensated by high-performance optical amplifiers.

V. Conclusion

We have presented an investigation of the benefits and tradeoffs of SL-MZMs with either lumped electrodes or TW electrodes.

We compared these two SL modulators to the C-MZM through calculation of their EO bandwidth and FOM, the latter being derived from the reduction of the static and dynamic TPPs. To this end, we developed a RLC circuit model to simulate the dynamic behavior of lumped-electrode SL-MZMs. Our model was validated with experimental measurement of an SL-MZM. Key findings are summarized below:

1) Due to the high loss and low bandwidth of the SL waveguides, the lumped-electrode SL-MZMs did not show any performance improvement over C-MZMs. In addition to the RC time constant, the interaction time between the lumped electrodes and the optical signal also limits the modulator speed. Simulations show that a C-MZM with a V_π of 7 V and a phase shifter length of $L_{C\text{-}MZM}$= 4.8 mm is characterized by an EO bandwidth of 15.8 GHz, while the lumped-electrode SL-MZM with the same V_π ($L_{SL\text{-}MZM}$= 4.8/γ mm) demonstrated a maximum EO bandwidth of 9 GHz.

2) SL-MZMs can offer remarkable benefits when implanted with TW electrodes. In this case, their EO bandwidth reaches 23 GHz at the optimum SL value of γ= 9 ($L_{SL\text{-}MZM}$= 533 µm). The FOM calculations show that the optimum SL-MZMs can then outperform C-MZMs at high-speed operations.

3) Furthermore, compared to the other strategies currently considered to reduce V_π of C-MZMs, employing the SL effect is the best-in-performance solution. Compared to the C-MZM, the optimized SL design allowed reducing the V_π from 7 V to 2.33 V, compacting the MZM arm length from 4.8 mm to 833 µm, improving EO bandwidth from 15.8 GHz to 17.6 GHz. These good performances are reached despite the additional loss of waveguides that can be compensated by an optical amplifier. Future progress in the design and fabrication process of SL waveguides should further reduce the propagation loss and make these modulators even more attractive for applications requiring arrays of high-speed, compact and energy efficient modulators.

APPENDIX I

The parameters of the lumped electrode, such as C_0, R_{PN}, C_{PN}, L, can be estimated using the measured S_{11} that is an all-electrical process. Indeed, these parameters can be extracted with curve fitting of the measured S_{11} and the back reflection formula of the TML, which is equal to R_{TML}=T_{TML}-*1*. In addition to that, there are numerical models to estimate their values. Under the reverse-bias operation, the capacitance and the series resistance of a p-n junction have been modeled in [25], [31], as shown in Fig. 16. The per-unit-length inductance of CPS is also approximated as [43],

$$L=\begin{cases}\dfrac{120}{V_{RF}}\ln\left(2\dfrac{1+\sqrt{K}}{1-\sqrt{K}}\right) & \dfrac{1}{\sqrt{2}}\le K\le 1\\[2ex] \dfrac{120\pi^2}{V_{RF}\ln\left[\dfrac{2\left(1+\sqrt{K'}\right)}{\left(1-\sqrt{K'}\right)}\right]} & 0\le K\le\dfrac{1}{\sqrt{2}}\end{cases}\quad [H/m] \tag{11}$$

$$K=\frac{s_{TML}}{s_{TML}+2w_{TML}},\qquad K'=\sqrt{1-K^2} \tag{12}$$

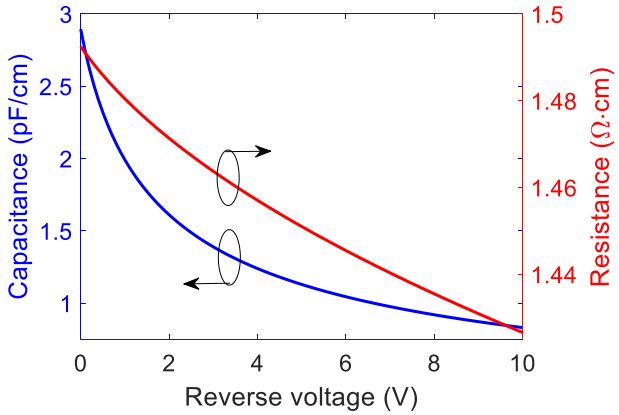

Fig. 16. Capacitance and resistance of PN junction as a function of the reverse bias.

where s_{TML} and w_{TML} are the distance between two metals and the width of the metals in a coplanar strip (CPS) TML, respectively. Moreover, C_0 is estimated to be around 26 fF [26].

All parameters with their vales that have been used in the simulation are listed in Table II.

APPENDIX II

Eq. (5) gives the phase shift in the time domain that is rewritten and solved in the frequency domain as

$$\Delta\varphi(V(\omega))=k_0\frac{C}{\gamma n_g}\mathbf{F}\Big[\Delta n_{eff}(V(t))*u(t) - \Delta n_{eff}(V(t))*u(t-t_0)\Big] \tag{13}$$

$$\Delta\varphi(V(\omega))=k_0\frac{C}{\gamma n_g}\left[\Delta n_{eff}(V(\omega))\times\left(\frac{1}{j\omega}+\pi\delta(\omega)\right)-\Delta n_{eff}(V(\omega))\times\left(\frac{1}{j\omega}+\pi\delta(\omega)\right)\times e^{-j\omega t_0}\right] \tag{14}$$

Table. II. A list of the parameters used in the simulation

Parameters	Notation	Values
Electrode inductance [nH]	L	0.167
Pad parasitic capacitance [fF]	C_0	26
impedance characteristic of the source [Ω]	Z_0	50
Characteristic impedance of the unloaded TML [Ω]	Z_{unload}	50
Capacitance of the TW electrode [pF/cm]	C_U	1.30
Inductance of the TW electrode [nH/cm]	L_U	6.33
p-n junction capacitance [pF/cm]	C_{PN}	Fig.16
p-n junction resistance [Ω.cm]	R_{PN}	Fig.16
Doping for n-dopants [cm^{-3}]	N_D	3×10^{17}
Doping for p-dopants [cm^{-3}]	N_A	5×10^{17}
Group index	n_g	3.8
Loss per enhancement factor for SL-MZMs [dB/cm]	$\alpha_{SL\text{-}MZM}$	17.5
Loss for the C-MZM [dB/cm]	$\alpha_{C\text{-}MZM}$	12.3
Optical wavelength [nm]	λ	1550

After some algebra, the Eq. (6) will be derived that represents direct expression of the phase shift as a function of the refractive index change in the frequency domain.

APPENDIX III

The amplitude response of MZMs at the quadrature point is given as

$$\left|S_{21}(\omega)\right|^2 = \mathbf{F}\left\{\exp(-\alpha L_{SL-MZM})\cos^2\left(\frac{\Delta\varphi(V,t)-\pi/2}{2}\right)\right\} \quad (15)$$

$$\left|S_{21}(\omega)\right|^2 = \mathbf{F}\left\{\frac{\exp(-\alpha L)}{2}\left(1+\cos\left(\Delta\varphi(V,t)-\pi/2\right)\right)\right\} \quad (16)$$

$$\left|S_{21}(\omega)\right|^2 = \mathbf{F}\left\{\frac{\exp(-\alpha L)}{2}\left(1+\sin\left(\Delta\varphi(V,t)\right)\right)\right\} \quad (17)$$

By excluding the DC component, Eq. (7) will be derived.

APPENDIX IV

The coupled equations of the forward and backward RF waves described in Ref. [31] is solved using the FDTD method as

$$\frac{V_F(z+1,t)-V_F(z,t)}{\Delta z_{RF}} + K_0\frac{V_F(z,t+1)-V_F(z,t)}{\Delta t} = -K_1\left[V_F(z,t)+V_R(z,t)-V_j(z,t)\right]-K_2V_{con}(z,t) \quad (18)$$

$$\frac{V_R(z+1,t)-V_R(z,t)}{\Delta z_{RF}} - K_0\frac{V_R(z,t+1)-V_R(z,t)}{\Delta t} = K_1\left[V_F(z,t)+V_R(z,t)-V_j(z,t)\right]-K_2V_{con}(z,t) \quad (19)$$

where V_F and V_R are the forward and the backward voltages, respectively. Δz_{RF} and Δt are the RF mesh size and the time step, respectively. The other terms are described as

$$K_0 = \frac{1}{2}\left[Z_{unload}C_U + \frac{L_U}{Z_{unload}}\right], \qquad K_1 = \frac{Z_{unload}}{2R_{PN}},$$
$$K_2 = \frac{1}{2}, \qquad K_3 = \left[Z_{unload}C_U - \frac{L_U}{Z_{unload}}\right] \approx 0 \quad (20)$$

$$V_{con}(z,t) = Z_{con}(t) * \left[\frac{V_R(z,t)-V_F(z,t)}{Z_{unload}}\right] \quad (21)$$

$$V_j(z,t+1) = \frac{V_F(z,t)+V_R(z,t)}{\Delta t + R_{PN}C_{PN}} + \frac{R_{PN}C_{PN}}{\Delta t + R_{PN}C_{PN}}V_j(z,t) \quad (22)$$

where Z_{unload}, C_U, and L_U represent the characteristic impedance, capacitor, and inductor of the unloaded TML, respectively. $Z_{con}(t)$ is the inverse Fourier transform of $Z_{con}(f)$ that represents the frequency-dependent conductor impedance [29], [31]. Also, the optical waves is numerically described as [31], [44]

$$E_F(z,t) = \exp\left\{\left[-\Delta\alpha(z-\Delta z_{Opt},t-\Delta t)/2 - i\Delta\beta(z-\Delta z_{Opt},t-\Delta t)\right]\Delta z_{Opt}\right\}E_F(z-\Delta z_{Opt},t-\Delta t) \quad (23)$$

where $\Delta\alpha$ and $\Delta\beta$ represent respectively the changes in the attenuation coefficient (Fig. 3, red line) and the propagation constant, due to the applied voltage.

ACKNOWLEDGMENT

This project was supported by Huawei Canada and the Natural Sciences and Engineering Research Council of Canada (CRDPJ 538381-18). The authors thank CMC Microsystems for the fabrication subsidy and MPW service.

REFERENCES

[1] J. Luo and A. K.-Y. Jen, "Highly Efficient Organic Electrooptic Materials and Their Hybrid Systems for Advanced Photonic Devices," *IEEE J. Sel. Top. Quantum Electron.*, vol. 19, no. 6, pp. 42–53, 2013.

[2] A. Chen and E. Murphy, *Broadband optical modulators: science, technology, and applications*. CRC press, 2011.

[3] M. Streshinsky *et al.*, "Highly linear silicon traveling wave Mach-Zehnder carrier depletion modulator based on differential drive," *Opt. Express*, vol. 21, no. 3, pp. 3818–3825, 2013.

[4] M. Streshinsky *et al.*, "Low power 50 Gb/s silicon traveling wave Mach-Zehnder modulator near 1300 nm," *Opt. Express*, vol. 21, no. 25, pp. 30350–30357, 2013.

[5] D. Patel *et al.*, "Design, analysis, and transmission system performance of a 41 GHz silicon photonic modulator," *Opt. Express*, vol. 23, no. 11, pp. 14263–14287, 2015.

[6] J. Zhou, J. Wang, L. Zhu, and Q. Zhang, "High Baud Rate All-Silicon Photonics Carrier Depletion Modulators," *J. Light. Technol.*, vol. 38, no. 2, pp. 272–281, 2020.

[7] R. Dubé-Demers, S. LaRochelle, and W. Shi, "Ultrafast pulse-amplitude modulation with a femtojoule silicon photonic modulator," *Optica*, vol. 3, no. 6, pp. 622–627, 2016.

[8] X. Zheng *et al.*, "A high-speed, tunable silicon photonic ring modulator integrated with ultra-efficient active wavelength control," *Opt. Express*, vol. 22, no. 10, pp. 12628–12633, 2014.

[9] Q. Xu, S. Manipatruni, B. Schmidt, J. Shakya, and M. Lipson, "12.5 Gbit/s carrier-injection-based silicon micro-ring silicon modulators," *Opt. Express*, vol. 15, no. 2, pp. 430–436, 2007.

[10] E. Timurdogan, C. M. Sorace-Agaskar, J. Sun, E. Shah Hosseini, A. Biberman, and M. R. Watts, "An ultralow power athermal silicon modulator," *Nat. Commun.*, vol. 5, no. 1, pp. 1–11, 2014.

[11] M. S. Hai, M. M. P. Fard, and O. Liboiron-Ladouceur, "A Ring-Based 25 Gb/s DAC-Less PAM-4 Modulator," *IEEE J. Sel. Top. Quantum Electron.*, vol. 22, no. 6, pp. 123–130, 2016.

[12] J. Sun, R. Kumar, M. Sakib, J. B. Driscoll, H. Jayatilleka, and H. Rong, "A 128 Gb/s PAM4 Silicon Microring Modulator With Integrated Thermo-Optic Resonance Tuning," *J. Light. Technol.*, vol. 37, no. 1, pp. 110–115, 2019.

[13] Y. Terada, K. Kondo, R. Abe, and T. Baba, "Full C-band Si photonic crystal waveguide modulator," *Opt. Lett.*, vol. 42, no. 24, pp. 5110–5112, 2017.

[14] T. Tatebe, T. Baba, Y. Hinakura, and Y. Terada, "Si Photonic Crystal Slow-Light Modulators with Periodic p–n Junctions," *J. Light. Technol.*, vol. 35, no. 9, pp. 1684–1692, 2017.

[15] T. Baba, H. C. Nguyen, N. Yazawa, Y. Terada, S. Hashimoto, and T. Watanabe, "Slow-light Mach–Zehnder modulators based on Si photonic crystals," *Sci. Technol. Adv. Mater.*, vol. 15, no. 2, p. 024602, 2014.

[16] S. Romero-García *et al.*, "High-speed resonantly enhanced silicon photonics modulator with a large operating temperature range," *Opt. Lett.*, vol. 42, no. 1, pp. 81–84, 2017.

[17] M. Passoni, D. Gerace, L. O'Faolain, and L. C. Andreani, "Slow light with interleaved p-n junction to enhance performance of integrated Mach-Zehnder silicon modulators," *Nanophotonics*, vol. 8, no. 9, pp. 1485–1494, 2019.

[18] C. Sciancalepore *et al.*, "Low-loss adiabatically-tapered high-contrast gratings for slow-wave modulators on SOI," in *High Contrast Metastructures IV*, 2015, vol. 9372, p. 93720G.
[19] R. Hosseini, L. Mirzoyan, and K. Jamshidi, "Energy Consumption Enhancement of Reverse-Biased Silicon-Based Mach–Zehnder Modulators Using Corrugated Slow Light Waveguides," *IEEE Photonics J.*, vol. 10, no. 1, pp. 1–7, 2018.
[20] A. Brimont *et al.*, "High-contrast 40 Gb/s operation of a 500 μm long silicon carrier-depletion slow wave modulator," *Opt. Lett.*, vol. 37, no. 17, pp. 3504–3506, 2012.
[21] O. Jafari, W. Shi, and S. Larochelle, "Mach-Zehnder Silicon Photonic Modulator Assisted by Phase-Shifted Bragg Gratings," *IEEE Photonics Technol. Lett.*, vol. 32, no. 8, pp. 445–448, 2020.
[22] X. Li, F. Yang, F. Zhong, Q. Deng, J. Michel, and Z. Zhou, "Single-drive high-speed lumped depletion-type modulators toward 10 fJ/bit energy consumption," *Photonics Res.*, vol. 5, no. 2, pp. 134–142, 2017.
[23] S. Sharif Azadeh, J. Nojić, A. Moscoso-Mártir, F. Merget, and J. Witzens, "Power-efficient lumped-element meandered silicon Mach-Zehnder modulators," *Silicon Photonics XV*, vol. 11285, p. 10, 2020.
[24] Y. Hinakura, Y. Terada, H. Arai, and T. Baba, "Electro-optic phase matching in a Si photonic crystal slow light modulator using meander-line electrodes," *Opt. Express*, vol. 26, no. 9, pp. 11538–11545, 2018.
[25] R. Dube-Demers *et al.*, "Analytical Modeling of Silicon Microring and Microdisk Modulators with Electrical and Optical Dynamics," *J. Light. Technol.*, vol. 33, no. 20, pp. 4240–4252, 2015.
[26] H. Yu *et al.*, "Performance tradeoff between lateral and interdigitated doping patterns for high speed carrier-depletion based silicon modulators," *Opt. Express*, vol. 20, no. 12, pp. 12926–12938, 2012.
[27] D. Samara-Rubio *et al.*, "Customized drive electronics to extend silicon optical modulators to 4 Gb/s," *J. Light. Technol.*, vol. 23, no. 12, pp. 4305–4314, 2005.
[28] G. L. Li, P. K. L. Yu, and T. G. B. Mason, "Analysis of Segmented Traveling-Wave Optical Modulators," *J. Light. Technol.*, vol. 22, no. 7, pp. 1789–1796, 2004.
[29] F. Cappelluti and G. Ghione, "Self-consistent time-domain large-signal model of high-speed traveling-wave electroabsorption modulators," *IEEE Trans. Microw. Theory Tech.*, vol. 51, no. 4, pp. 1096–1104, 2003.
[30] H. Yu and W. Bogaerts, "An equivalent circuit model of the traveling wave electrode for carrier-depletion-based silicon optical modulators," *J. Light. Technol.*, vol. 30, no. 11, pp. 1602–1609, 2012.
[31] H. Bahrami, H. Sepehrian, C. S. Park, L. A. Rusch, and W. Shi, "Time-Domain Large-Signal Modeling of Traveling-Wave Modulators on SOI," *J. Light. Technol.*, vol. 34, no. 11, pp. 2812–2823, 2016.
[32] O. Jafari, H. Sepehrian, S. LaRochelle, and W. Shi, "High-Efficiency Silicon Photonic Modulator Using Coupled Bragg Grating Resonators," *J. Light. Technol.*, vol. 37, no. 9, pp. 2065–2075, 2019.
[33] L. Chrostowski and M. E. Hochberg, *Silicon photonics design*. Cambridge University Press, 2015.
[34] H. Sepehrian, A. Yekani, W. Shi, and L. A. Rusch, "Assessing performance of silicon photonic modulators for pulse amplitude modulation," *IEEE J. Sel. Top. Quantum Electron.*, vol. 24, no. 6, pp. 1–10, 2018.
[35] H. Sepehrian, J. Lin, L. A. Rusch, and W. Shi, "Silicon Photonic IQ Modulators for 400 Gb/s and Beyond," *J. Light. Technol.*, vol. 37, no. 13, pp. 3078–3086, 2019.
[36] S. Hughes, L. Ramunno, J. F. Young, and J. E. Sipe, "Extrinsic Optical Scattering Loss in Photonic Crystal Waveguides: Role of Fabrication Disorder and Photon Group Velocity," *Phys. Rev. Lett.*, vol. 94, no. 3, pp. 033903–6, 2005.
[37] C. Monat *et al.*, "Slow light enhancement of nonlinear effects in silicon engineered photonic crystal waveguides," *Opt. Express*, vol. 17, no. 4, pp. 2944–2953, 2009.
[38] E. Timurdogan *et al.*, "400G Silicon Photonics Integrated Circuit Transceiver Chipsets for CPO, OBO, and Pluggable Modules," in *Optical Fiber Communication Conference (OFC)*, 2020, p. T3H.2.
[39] H. Sepehrian, A. Yekani, L. A. Rusch, and W. Shi, "CMOS-Photonics Codesign of an Integrated DAC-Less PAM-4 Silicon Photonic Transmitter," *IEEE Trans. Circuits Syst. I Regul. Pap.*, vol. 63, no. 12, pp. 2158–2168, Dec. 2016.
[40] N. Qi *et al.*, "Co-Design and Demonstration of a 25-Gb/s Silicon-Photonic Mach-Zehnder Modulator with a CMOS-Based High-Swing Driver," *IEEE J. Sel. Top. Quantum Electron.*, vol. 22, no. 6, pp. 131–140, 2016.
[41] B. Casper *et al.*, "A 112 Gb/s PAM4 Silicon Photonics Transmitter With Microring Modulator and CMOS Driver," *J. Light. Technol.*, vol. 38, no. 1, pp. 131–138, 2020.
[42] V. Stojanović *et al.*, "Monolithic silicon-photonic platforms in state-of-the-art CMOS SOI processes [Invited]," *Opt. Express*, vol. 26, no. 10, pp. 13106–13121, 2018.
[43] C. R. Paul, *Inductance : loop and partial*. Wiley, 2010.
[44] K. Kiziloglu, N. Dagli, G. L. Matthaei, and S. I. Long, "Experimental Analysis of Transmission Line Parameters in High-Speed Gaas Digital Circuit Interconnects," *IEEE Trans. Microw. Theory Tech.*, vol. 39, no. 8, pp. 1361–1367, 1991.

Omid Jafari received the M.Sc. degree in electrical engineering (Microwave Photonic) from Sharif University of Technology, Tehran, Iran, in 2014. He is currently working toward his Ph.D. degree at the Centre for Optics Photonics, and Lasers (COPL), ECE Department, Université Laval, QC, Canada. His research interests include nano-/micro-photonic devices, CMOS-photonics co-design, and high-speed optical communications.

Wei Shi (S'07–M'12) is an Associate Professor with the Department of Electrical and Computer Engineering, Université Laval, Québec, Canada and holds a Canada Research Chair in Silicon Photonics. He received the Ph.D. degree in electrical and computer engineering from the University of British Columbia, Vancouver, Canada. Before joining Université Laval in 2013, he was a researcher at McGill University, Montreal, QC, Canada, where he held a Postdoctoral Fellowship from the Natural Sciences and Engineering Research Council of Canada (NSERC). His current research focuses on integrated photonic devices and systems, involving silicon photonics, nanophotonics, CMOS-photonics co- design, high-speed optical communications, chip-scale lasers, and optical sensors. He is a senior member of OSA and a member of IEEE and the Center for Optics, Photonics (COPL).

Sophie LaRochelle (M'00, SM'13) received a Bachelor's degree in engineering physics from Université Laval, Canada, in 1987; and a Ph.D. degree in optics from the College of Optical Sciences, University of Arizona, USA, in 1992.
From 1992 to 1996, she was a Research Scientist at the Defense Research and Development Canada - Valcartier, where she worked on electro-optical systems. Since 1996, she is a professor at the Department of Electrical and Computer Engineering, Université Laval, where she holds a Canada Research Chair (Tier 1) in Advanced Photonic Technologies for Communications. Her current research activities are focused on optical fibers and integrated devices for optical communication systems including silicon photonic modulators and filters, optical fiber designs for space division multiplexing and multi-core multi-mode amplifiers. Over the years, Dr LaRochelle has made highly cited contributions to the fields of fiber Bragg gratings, fiber lasers, optical CDMA and optical signal processing. She has published more than 400 papers in peer-reviewed journals and conferences. Dr. LaRochelle is an IEEE senior member (2013) and an OSA Fellow.